

Minerva Access is the Institutional Repository of The University of Melbourne

Author/s:

Corletto, A;Shapter, JG

Title:

Thickness/morphology of functional material patterned by topographical discontinuous dewetting

Date:

2021-09

Citation:

Corletto, A. & Shapter, J. G. (2021). Thickness/morphology of functional material patterned by topographical discontinuous dewetting. NANO SELECT, 2 (9), pp.1723-1740. <https://doi.org/10.1002/nano.202000301>.

Persistent Link:

<https://hdl.handle.net/11343/289574>

License:

[CC BY](#)

RESEARCH ARTICLE

Thickness/morphology of functional material patterned by topographical discontinuous dewetting

Alexander Corletto  | Joseph G. Shapter 

Australian Institute for Bioengineering and Nanotechnology, The University of Queensland, Brisbane, Queensland, Australia

Correspondence

Joseph G. Shapter, Australian Institute for Bioengineering and Nanotechnology, The University of Queensland, St. Lucia, Brisbane, QLD 4072, Australia.
Email: j.shapter@uq.edu.au

Abstract

Topographical discontinuous dewetting (TDD) patterning is a nascent 2D printing technique explored for high-throughput nanoscale patterning of functional material inks. However, variables affecting the z thickness and morphology of the deposited functional materials inside the patterned microchannels remain unexplored. We developed a theoretical model that can determine the thickness of the deposited functional material layers using the TDD patterning technique. We then confirmed the model with experimental data by depositing colloidal dispersions into microchannels using TDD patterning to systematically study the effects of different processing variables. The contribution of evaporation-driven flow to the deposited layer thickness was significant, with the relationship of thickness to inking speed different to that previously determined for thin film blade coating of colloidal dispersions in the evaporative regime. Additionally, a viscosity dampening effect was observed, unique to TDD of microchannels, which slowed the evaporation-driven flow due to local viscosity increase in the microchannels. Channel dimensions and ink dispersion concentration affected thickness as hypothesized. Internal flows in the microchannels normal to the sidewalls and perpendicular to the microchannel length (“coffee ring” effect capillary flow/Marangoni flow) were found to contribute significantly to the final morphology/thickness of the deposited layers for the systems/dispersions experimentally measured.

KEYWORDS

conductive inks, functional inks, nanoscale patterning, selective wetting, self-assembly

1 | INTRODUCTION

Topographical discontinuous dewetting (TDD) is being explored by researchers as an effective template-guided, self-assembly, nanoscale/microscale patterning and 2D printing technique for a variety of different functional

materials including nanomaterials,^[1–4] polymers,^[5,6] biomaterials,^[7] organic single crystals,^[1,8–13] and perovskite.^[14] Discontinuous dewetting occurs due to variations in the wettability of a substrate surface. Controlling the areas of wettability allows researchers to pattern functional material inks onto the substrate,

This is an open access article under the terms of the [Creative Commons Attribution](https://creativecommons.org/licenses/by/4.0/) License, which permits use, distribution and reproduction in any medium, provided the original work is properly cited.

© 2021 The Authors. *Nano Select* published by Wiley-VCH GmbH

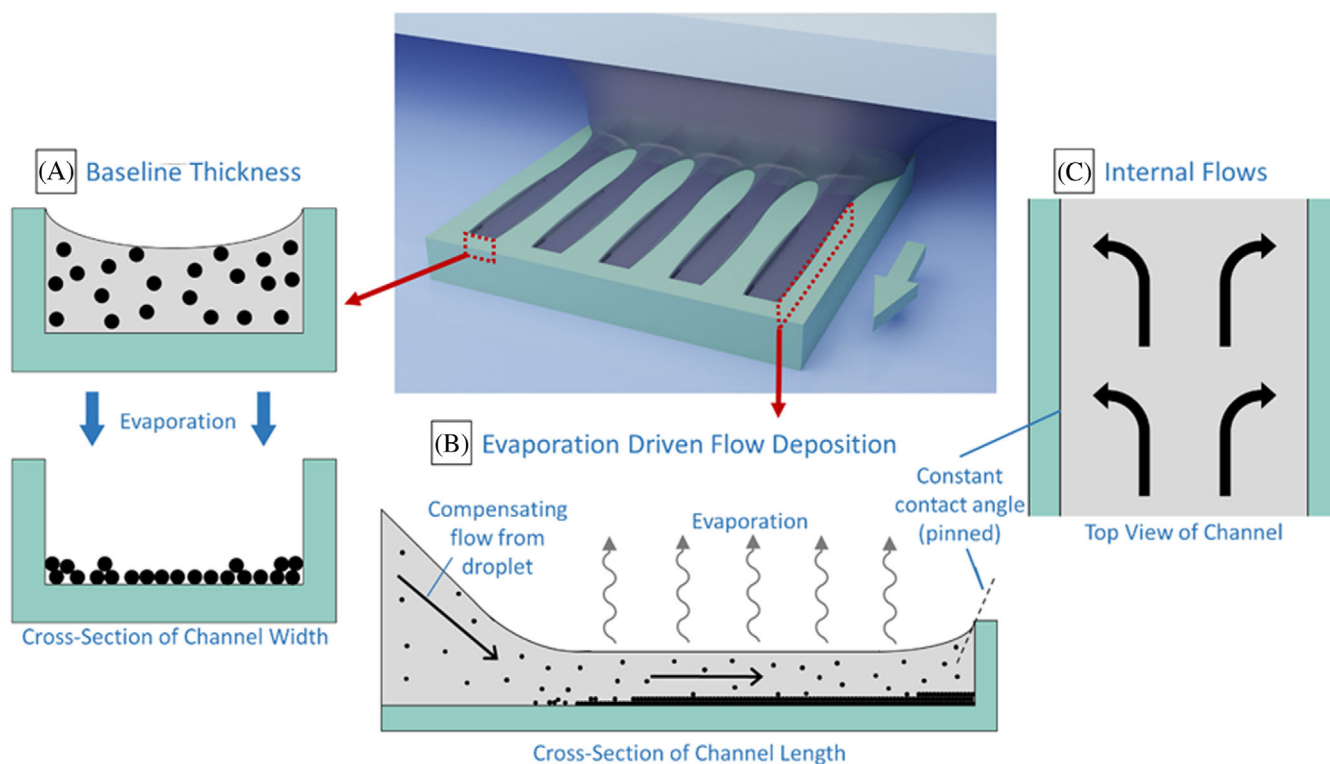


FIGURE 1 TDD patterning of microchannels. Different phenomena contribute to the resulting thickness and morphology of the deposited layers in the microchannels. **(A)** Baseline thickness of the deposited layer, T_0 . Obtained from the ink material depositing after evaporation from the ink droplet volume pinned in the microchannel. **(B)** Additional ink material deposited from evaporation-driven flow. Evaporation of ink solvent along the microchannel surface and a pinned contact line at the top edge of the microchannels results in a compensating flow due to the pressure gradient, bringing additional ink material into the microchannel from the dragged droplet. **(C)** Internal flows including the capillary flow from the coffee-ring effect and Marangoni flows can alter the distribution of deposited material in the microchannel. These flows generally move ink material towards the sidewalls and creates deposited layers with concave morphology.

which when dried, deposit the target materials into desired patterns. Controlling the wettability can be done by controlling the chemistry of the substrate surface to make hydrophilic/hydrophobic patterns, and this has been researched extensively.^[15–18] However, the wettability can also be controlled by the substrate surface topography. “Topographical” discontinuous dewetting (TDD) has been used to selectively fill patterned, open cavities with functional inks, depositing the functional materials into the open cavities in desired patterns.^[7] The deposited solidified materials in cavities can be transferred to target substrates using liquid bridge transfer, allowing multiple patterned layers fabricated on the same substrate with potential roll-to-roll (R2R) compatibility.^[1,3,4,11] The 2D printing technique of TDD is a form of intaglio printing like gravure printing, except uses innovative manipulation of the ink/surface interactions and surface topography to control deposition into the patterned cavities rather than removing excess ink with a doctor blade. An important advantage for TDD is that nanoscale lateral resolution is readily achievable,^[1] unlike gravure printing,^[19,20] with

well-defined line edges. The channel walls also allow TDD to more easily achieve thicker features compared to other patterning techniques, as well as improve particle deposition uniformity within the central region of the patterned features.^[21] The technique can be done with low energy, low temperature, and low cost, and has consequently been used for a variety of applications including field-effect transistors,^[1,8,13] and electrodes,^[2,3] for computing and sensors.

TDD involves dragging an ink dispersion droplet over a substrate that has an array of patterned cavities indented into the surface (Figure 1).^[7] If the receding contact angle (RCA) of the ink droplet on the printing substrate surface is controlled within a certain range then the ink will selectively fill the cavities and completely dewet from the upper non-cavity surface. Selective filling of the cavities occurs due to the ink droplet three-phase contact line pinning at the cavity top edge as the droplet moves over the cavities. The contact angle abruptly increases at the cavity edge due to the surface plane rotating sharply at the cavity sidewall, which results in a higher contact angle

than the critical RCA and pins the three-phase contact line. Functional materials solvated or dispersed in the ink will be selectively deposited into the patterned cavities when the pinned ink droplet solvent evaporates. Knowing the conditions that ensure effective and consistent TDD and the effect of different conditions on the morphology of the resulting deposited layer is critical to realize commercial use of this patterning technique for fabricating advanced functional devices. Patterns of functional materials printed must have reliably controlled and consistent properties to ensure the reliability and quality of the fabricated devices.

Previous work by Deagen et al. has explained and tested conditions that ensure effective TDD for rectangular open microchannel cavities that avoids residual films on the non-cavity substrate surface (unwanted Landau–Levich deposition regime) and uncontrolled ink depinning from the microchannels.^[6] While the lateral dimensions of the deposited layers are firmly controlled by the channel dimensions, the z thickness and top surface curvature depend directly on the conditions of the patterning process. However, how these conditions affect the z thickness and top surface curvature for patterns has not been explored and determined, even though controlling these is critical for different applications. Obtaining thicker pattern features can increase the conductivity of electrodes/interconnects fabricated with this technique while keeping the lateral area use constant. This can lower the sheet resistance for transparent conductive electrodes and reduce the required interconnect/electrode area usage for printable electronics. Conversely, thinner pattern features may be required to apply thin coatings in the microchannels, create multilayer stack structures, keep transparency high, or maintain semiconducting characteristics.^[22] Nanometer film thickness variations can even change a film's interface properties. For example, Nafion thin films change from hydrophobic to hydrophilic when thickness is $< \sim 55$ nm.^[23] Either way, thickness and morphology of the deposited layer must be reliably controlled to ensure consistent properties from device to device. This is especially important for electronics where resistance needs to be consistent to ensure correct current and voltage throughout the devices.

This work explores for the first time the variables that can affect the thickness and morphology of the deposited layers formed from depositing functional materials through TDD into microscale channels. We propose the first theoretical model to determine the resulting deposited layer thickness and obtained experimental data to verify the model. Inking blade speed, microchannel dimensions and pitch, and ink dispersion concentration were varied when depositing Nafion polymer dispersions into PDMS channels to experimentally determine the changes to deposited layer morphology. Deposited

layer morphology was characterized by scanning electron images (SEM) of microchannel cross sections. We found that the contribution of evaporation-driven flow to the deposited layer thickness was significant with the thickness generally related to the meniscus dwell time per unit length (inverse of inking speed). An additional viscosity/aggregation dampening effect was observed that slowed the evaporation-driven flow over time due to local increase in viscosity in the microchannels. Deposited layer thickness increased linearly with dispersion concentration as hypothesized. Increasing microchannels width and depth resulted in a decreased or increased deposited layer thickness, respectively. This is partly due to change in flow profile and the change in the effect of internal flows like Marangoni and capillary flows due to microchannel geometry. Interestingly, we found increasing microchannel pitch decreased thickness due to cumulative lowering of pressure within the dragged dispersion droplet near adjacent microchannels, and consequently a decreased evaporation-driven pressure gradient. The microchannels result has fundamentally different deposition dynamics than other studied systems like blade coating film deposition in the evaporative regime. This is because contact line pinning occurs due to patterned substrate topography resulting in a different complex meniscus morphology and flow dynamics.

2 | THEORY AND MODELING

During TDD of microchannels, we propose there are three main contributions that affect the z thickness and morphology of the deposited layers in the microchannels. The first contribution is from the volume of ink that is pinned inside the microchannel (Figure 1A). Any material solvated/dispersed in that pinned volume of ink will eventually deposit into the microchannel after solvent evaporation and form the deposited layers. This volume depends on the channel dimensions as well as the contact angle of the ink on the channel sidewalls which determines the curvature of the pinned droplet top surface. This contribution should always be present during TDD, and can be considered the baseline quantity of material in the deposited layer (baseline layer thickness, T_0).

The second contribution to the deposited layer is from the evaporation-driven flow or convective flow,^[24] similar to what occurs in capillary printing^[25–28] and an effect we encountered when patterning single-walled carbon nanotubes (SWCNTs) using TDD.^[4] The stretched ink droplet pinned in the microchannels has an increased open surface area that increases evaporation of the ink solvent in the microchannels. As the solvent evaporates, a pressure gradient develops which causes more ink to flow from the

main droplet down into the microchannels, carrying more material into the microchannels (Figure 1B). This is essentially the “coffee ring” effect where liquid flows towards a pinned contact line as the droplet evaporates.^[29] The evaporation-driven flow is inhibited by the viscosity of the ink^[30] and so higher viscosity inks will have no or negligible contribution to the deposited layer morphology from this flow.

The third contribution to the morphology of the deposited layer is the internal (perpendicular) flows of the ink in the microchannels during evaporation (Figure 1C).^[31] As the ink contact line is pinned to the microchannel top edges, any evaporation will cause an outward flow towards the sidewalls of the channels to compensate for depleted volume, again a cavity-pinned “coffee ring” effect. This outward flow towards the sidewalls has similarly been previously reported in evaporating dispersions within open microchannels.^[30,32] Solvent mixtures in the ink solution/dispersion can also cause Marangoni flows toward the sidewall or the center of the microchannel depending on the solvent properties.^[31,33,34] These flows will generally cause more material to be deposited near the sidewalls of the channels, resulting in a convex surface morphology of the deposited layer in the microchannels, and thinner layer in the middle of the microchannel. Again, this contribution will decrease with increased ink viscosity.

2.1 | Theoretical model for determination of deposited layer thickness

The total particle volume in the deposited layer for a length of channel dl is equal to the sum of the baseline particle volume deposited (Figure 1A) and the particle volume deposited through evaporation-driven deposition (Figure 1B).

$$\begin{aligned} \text{Deposited layer Volume} &= \text{Baseline Volume deposited} \\ &+ \text{Evap. driv. flow Volume deposited} \end{aligned}$$

which can be calculated as

$$A_{dep} \varphi_{\max} dl = A_{ch} \varphi_0 dl + Q_{ev} \varphi_0 D dl \quad (1)$$

Where A_{dep} and A_{ch} are the cross-sections of the deposited layer and the pinned droplet in the channel, respectively, φ_{\max} is the maximum packing volume fraction of the solid ink material, φ_0 is the initial volume fraction of the solid ink material in dispersion, Q_{ev} is the evaporation-driven volumetric flow of ink dispersion from the main droplet into the microchannel, D is the dwell

time per unit length (inverse of the inking speed), and dl is per length of microchannel. Assuming laminar flow in the microchannels due to the small diameter, we can use the Darcy–Weisbach equation,

$$\frac{\Delta p}{L} = \frac{32 \rho v^2}{Re D_H} \quad (2)$$

and substituting in the full terms of the Reynolds number $Re = \frac{v \rho L^*}{\eta(\varphi)}$ and substituting the average flow velocity v as Q_{ev} divided by A_{ch} , we can obtain an equation for Q_{ev} ,

$$Q_{ev} = \frac{A_{ch} L^* D_H}{32} \frac{\Delta p}{\eta(\varphi) L} = \frac{k_A \Delta p}{\eta(\varphi) L} \quad (3)$$

where Δp is the evaporation-driven pressure gradient in the microchannel, $\eta(\varphi)$, is the viscosity of the dispersion in the microchannel, L is the length of channel which evaporation and evaporation-driven flow is occurring, D_H is the hydraulic diameter, L^* is the characteristic length in the Reynolds number, and k_A we define as the microchannel geometry constant for the evaporation-driven flow of dispersion into the microchannels. Flow in microchannels has been found in the literature to have L^* of the root of the cross-sectional area (\sqrt{A}),^[35–37] and D_H for open rectangular channels is $\frac{4A}{2d+w}$ where d and w are depth and width of the microchannel, respectively and A is the cross-sectional area of the flow. Substituting into the microchannel geometry constant,

$$k_A = \frac{A_{ch} L^* D_H}{32} = \frac{A_{ch}^{5/2}}{16d + 8w} = \frac{(\langle h \rangle w)^{5/2}}{16d + 8w} \quad (4)$$

where, $\langle h \rangle$ is the average of the channel-pinned droplet height. Note that $\langle h \rangle = d$ when the pinned droplet has a perfectly flat top surface (90° contact angle with respect to sidewall surface), but $\langle h \rangle < d$ when the pinned droplet has some curvature surface ($<90^\circ$ contact angle with respect to sidewall surface). Substituting Equation 3 into Equation 1 results in,

$$A_{dep} \varphi_{\max} dl = A_{ch} \varphi_0 dl + \frac{k_A \Delta p \varphi_0 D dl}{\eta(\varphi) L} \quad (5)$$

Dividing both sides by the channel width (w) and length portion (dl) results in

$$\langle T \rangle \varphi_{\max} = \langle h \rangle \varphi_0 + \frac{k_A \Delta p \varphi_0 D}{\eta(\varphi) L w} \quad (6)$$

where $\langle T \rangle$ is the average of the deposited layer thickness. Δp is proportional to the exposed surface area of the

channel section ($L.w$), and so can be presented as

$$p_{ev} = \frac{\Delta p}{L w} \propto \text{Evaporation rate} \quad (7)$$

where the constant evaporation-induced pressure gradient per surface area (p_{ev}) is proportional to the standard evaporation rate (generally presented as per area). Equation 6 is then,

$$\langle T \rangle \varphi_{max} = \langle h \rangle \varphi_0 + \frac{k_A p_{ev} \varphi_0 D}{\eta_{(\varphi)}} \quad (8)$$

The ink viscosity in the channel $\eta_{(\varphi)}$ is dependent on φ , which is dependent on Q_{ev} , which in turn is dependent on $\eta_{(\varphi)}$. We used the relation $\eta_{(\varphi)} = A_\eta \varphi^k$ for the viscosity where A_η and k are an experimentally-determined coefficient and power factor, respectively. This relation is consistent with the literature on experimental analysis of different dispersions including Nafion dispersions similar to the dispersions we use in this work.^[38] This relation can capture many different dispersions' viscosity to concentration profiles by incorporating these experimentally-determined parameters. However, φ in the microchannels is dependent on Q_{ev} due to ink dispersion flowing into the microchannel adding dispersion particles into the same microchannel volume. Incorporating the change in $\eta_{(\varphi)}$ due to Q_{ev} , we derive,

$$\eta_{(\varphi)} = A_\eta \left(\varphi_0 + \varphi_0 \frac{k_A p_{ev} D}{\eta_0 \langle h \rangle} \right)^k \quad (9)$$

where η_0 is the initial viscosity of the ink dispersion (see Supporting Information 1 for full derivation). Substituting into Equation 8 results in,

$$\langle T \rangle = \frac{\varphi_0}{\varphi_{max}} \left(\langle h \rangle + \frac{k_A p_{ev} D}{A_\eta \left(\varphi_0 + \varphi_0 \frac{k_A p_{ev} D}{\eta_0 \langle h \rangle} \right)^k} \right) \quad (10)$$

Finally, the actual deposited layer thickness T at the center of the microchannels will deviate from the average thickness $\langle T \rangle$ due to perpendicular fluid flows in the microchannel like Marangoni flows and capillary flows that direct the ink material within the microchannels towards the sidewalls or the center, perpendicular to the channel length, before deposition (Figure 1C). We include this deviation from $\langle T \rangle$ due to the internal flows as C , the internal flow factor,

$$T = \frac{\varphi_0 C}{\varphi_{max}} \left(\langle h \rangle + \frac{k_A p_{ev} D}{A_\eta \left(\varphi_0 + \varphi_0 \frac{k_A p_{ev} D}{\eta_0 \langle h \rangle} \right)^k} \right) \quad (11)$$

Minimal literature discusses the effect of these flows on particle deposition inside cavities. However, Okuzono et al. presented a theoretical model to describe the final shape of a polymer film deposited from a polymer solution drying within a cavity (enclosed by banks) on a substrate.^[39] Applying this model to the current work of functional material dispersion drying in cavities can incorporate the effect of the perpendicular Marangoni/capillary flows on the final deposited layer thickness at the center of the microchannel. Deriving T from the model (see Supporting Information 2 for full derivation) results in

$$T = \frac{(\varphi_0 h_f)^{3/2}}{\varphi_{max} \sqrt{\varphi_g h_0}} \quad (12)$$

where h_0 is the height of the pinned droplet in the microchannel at the microchannel center before evaporation, φ_g is the particle volume fraction of the ink dispersion when "gelation" occurs, and h_f is equivalent to,

$$h_f = \left(\langle h \rangle + \frac{k_A p_{ev} D}{A_\eta \left(\varphi_0 + \varphi_0 \frac{k_A p_{ev} D}{\eta_0 \langle h \rangle} \right)^k} \right) \quad (13)$$

Gelation occurs when viscosity sharply increases at a certain φ and any flow within the ink dispersion essentially stops. φ_g is determined experimentally. If the model presented by Okuzono et al. applies to the experimentally studied system in this current work, then Equation 12 should be equal to Equation 11,

$$\frac{\varphi_0 h_f C}{\varphi_{max}} = \frac{(\varphi_0 h_f)^{3/2}}{\varphi_{max} \sqrt{\varphi_g h_0}} \quad (14)$$

and consequently we can determine the internal flow factor C ,

$$C = \sqrt{\frac{\varphi_0 h_f}{\varphi_g h_0}} \quad (15)$$

where $0 < C \leq 1$. Note that C also depends on h_f . Substituting Equation 15 back into Equation 11 we finally obtain the model to determine thickness T of the deposited layer in the microchannels due to TDD,

$$T = \frac{\varphi_0^{3/2}}{\varphi_{max} \sqrt{\varphi_g h_0}} \left(\langle h \rangle + \frac{k_A p_{ev} D}{A_\eta \left(\varphi_0 + \varphi_0 \frac{k_A p_{ev} D}{\eta_0 \langle h \rangle} \right)^k} \right)^{3/2} \quad (16)$$

We use Equation 16 as a mathematical model to determine the deposited layer thickness in the microchannels

during TDD patterning. To fit the model to the obtained experimental data, we expand Equation 16 as a Taylor series at $D = 0$ to two terms as a good approximation of the function,

$$T^{2/3} = \frac{\varphi_0}{\sqrt[3]{\varphi_{\max}^2 \varphi_g h_0}} \times \left(\langle h \rangle + \frac{k_A p_{ev}}{A_\eta \varphi_0^k} D - \frac{k k_A^2 p_{ev}^2}{A_\eta \varphi_0^k \eta_0^2 \langle h \rangle} D^2 \right) \quad (17)$$

Equation 17 is now in a quadratic form with respect to D and we will fit our experimental data with varying D to a quadratic function to determine the fit of the model to the data. Additionally, Equation 11 can be expanded as a Taylor series at $D = 0$ to two terms to compare observe trends without using the Okuzono et al. model to determine C ,

$$T = \frac{\varphi_0 C}{\varphi_{\max}} \left(\langle h \rangle + \frac{k_A p_{ev}}{A_\eta \varphi_0^k} D - \frac{k k_A^2 p_{ev}^2}{A_\eta \varphi_0^k \eta_0^2 \langle h \rangle} D^2 \right) \quad (18)$$

2.2 | Limits of the model

We propose some theoretical limits to the change in layer thickness due to the inking speed. At maximum inking speed where meniscus dwell time per unit length approaches zero ($D \rightarrow 0$), there should be negligible additional evaporation-driven deposition as there is negligible time for the evaporation-driven flow to occur. This should result in the final deposited layer thickness approximately equal to the baseline layer thickness T_0 (Figure 1A),

$$T_0 = \frac{\varphi_0 C}{\varphi_{\max}} \langle h \rangle = \frac{\varphi_0^{3/2}}{\varphi_{\max} \sqrt{\varphi_g h_0}} \langle h \rangle^{3/2} \quad (19)$$

T_0 will depend on the maximum packing volume fraction of the particles deposited from dispersion (φ_{\max}), and the effect on thickness due to internal flows in the microchannels during solvent evaporation (internal flow factor, C). Any imperfect packing of the dispersion particles ($\varphi_{\max} < 1$) will result in an increase of T_0 due to the deposited layer volume also incorporating additional void volume between the stacked particles. T_0 is also generally lowered due to the effect of internal flows C to the microchannel sidewalls during evaporation (Marangoni/capillary), as they generally remove material from the center of the channel where thickness is measured and results in a convex top surface morphology.

Y-intercept of the deposited layer thickness model in Equation 11 should then simply be equal to the baseline thickness T_0 when ignoring thickness devia-

tion due to internal flows and assuming perfect packing ($\varphi_{\max} = C = 1$). For our experimental data, the 5% w/v Nafion dispersion with Nafion density $\sim 0.924 \text{ g mL}^{-1}$ had $\varphi_0 = \sim 0.0539$, meaning T_0 should be a maximum $\sim 5.39\%$ of the channel depth if there is perfect packing with no internal flows. The actual T_0 /channel depth is generally lowered due to C and increased if there is imperfect packing of the deposited particles ($\varphi_{\max} < 1$). Our data using deposited Nafion polymer that has been heated will generally result in better packing (higher φ_{\max}) compared to using harder particle dispersions like metal nanoparticles.

Maximum inking speed is also limited by the TDD process, as inking speeds over the maximum will leave a residual film or droplets on the non-cavity areas. This transition into leaving of a residual film at higher inking speeds is essentially the onset of the Landau–Levich deposition regime,^[40–42] which is to be avoided during TDD to ensure effective patterning.^[6] Maximum inking speed may still result in some minimum but non-zero amount of evaporation-driven flow, depending on other conditions.

At the minimum inking speed where meniscus dwell time per unit length becomes very long, evaporation-driven flow could continue until the microchannels fill up to a maximum thickness where the TDD process fails due to the change in topography of the microchannel. It is also possible that the microchannels overflow and render the patterning process ineffective. The maximum layer thickness should for this case depend on the channel dimensions, the contact angle of the ink on the channel wall, and potentially the properties of the deposited layer material. The maximum layer thickness is also limited by the local change in ink particle volume fraction due to the evaporation-driven flow. If there is an evaporation-driven flow that is transporting extra material from the main ink droplet into the microchannel, and the material is not depositing onto the microchannel surface as quickly as new material is arriving in the local region of the microchannel, then material concentration in the ink within the microchannels will increase locally. Increasing material concentration in colloidal dispersions generally increases the viscosity of the dispersion.^[41,43] We confirmed this for the Nafion colloidal dispersions used for our deposited layer thickness experiments. Figure 2 displays the viscosity against shear rate for the pure binary solvent, the standard 5% w/v Nafion dispersion, and a 16.4% w/v concentrated Nafion dispersion prepared by simple evaporation of the standard 5% w/v dispersion to mimic the effect of solvent evaporation in the microchannels. Viscosity increased for the higher concentration Nafion dispersion, with values similar to recent literature.^[38]

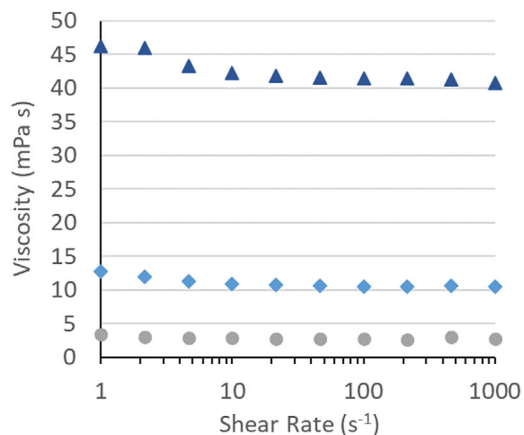


FIGURE 2 Plots of measured viscosity against shear rate for pure binary solvent mixture (grey spheres), 5.16% w/v Nafion dispersion (light blue diamonds), and the evaporation concentrated 16.4% w/v Nafion dispersion (dark blue triangles).

Local concentration increases of the dispersion in the microchannels can locally increase the viscosity which gradually decreases the evaporation-driven flow into the microchannels resulting in a viscosity dampening effect. Local viscosity dampening of the evaporation-driven flow can continuously increase as the flow increases the local concentration until the evaporation-driven flow essentially stops. Increasing aggregation of particles in locally concentrated dispersions can also block additional evaporation-driven flow. Particles that deposit from solution/dispersion faster on to the microchannel surface will decrease the local viscosity dampening and local aggregation allowing increased evaporation-driven flows. Local viscosity/aggregation dampening, which both change with time, will limit the maximum evaporation-driven deposition in the microchannels and thus limit the maximum layer thickness obtainable. The local viscosity/aggregation dampening should continuously decelerate evaporation-driven flows as dwell time per unit length increases. Our model in Equation 17 incorporates this decelerating viscosity/aggregation dampening component as there is a negative square term for D . Evaporation-driven flows will also be negligible or non-existent for high viscosity inks where flow is restricted. This trend has limits in terms of the range where it is accurate. The trend ends when the slope goes to zero, as the viscosity dampening effect would stop when evaporation-driven flow is zero. The trend also ends when the inking speed is fast enough that no evaporation-driven flow occurs or the TDD process fails.

2.3 | Applicability of the model

The model in Equations 11 or 16 is applicable to any dispersion of functional materials that is used as an

ink for TDD patterning. The model already incorporates the important properties of the dispersion that may vary between different functional material dispersions and which may influence the TDD process. Some applicable functional material dispersions that may be of interest include conductive polymer dispersions like poly(3,4-ethylenedioxythiophene) polystyrene sulfonate (PEDOT:PSS), polyaniline, and polypyrrole, and nanomaterial dispersions like SWCNTs, graphene, and metal nanoparticles. However, the incorporation of the model by Okuzono et al. to determine the internal flow factor C depends on the particles in the ink dispersion flowing regularly and continuously with the solvent.^[39] Some ink dispersions can have particles that do not flow regularly with the solvent and the coffee-ring effect or the effect of Marangoni flows is suppressed. This is particularly apparent for longer, higher aspect ratio particles or fibres/wires.^[44] In this case, the model by Okuzono et al. may not be as applicable and Equation 11 should be used as the model with C determined through other methods including experimentally. Properties of functional material dispersion will need to be characterized to accurately predict the deposited layer thickness using the model, including concentration-dependent viscosity, evaporation rate, particle volume fraction, maximum packing volume fraction, and others.

The model is applicable to a particular range of microchannel dimensions also. Microchannels too wide and deep will result in gravitational forces dominating surface tension and prevent droplet pinning within the microchannel. Maximum widths/depths may be in the millimeter range but will vary depending on the properties of the ink dispersion. Conversely, minimum widths/depths of the channel will depend on the scale of the dispersed particles. Channels that are too small will physically hinder the particles from entering and depositing in the channels.

3 | RESULTS AND DISCUSSION

Our aim was to determine the variables that affect the thickness of material layers deposited in microscale channels during TDD and observe trends in the variables that determine the relationships between the inking variables and the deposited layer thickness. An understanding of these relationships is critical to control the deposited layer thickness and morphology when using TDD for micro/nanoscale patterning. We deposited Nafion dispersions in microchannels in PDMS substrates using TDD under varying conditions and microchannel dimensions to experimentally verify the theoretical model proposed. Nafion dispersion was used as model ink dispersion as

it is a well understood colloidal polymer dispersion and scalable micro/nanoscale patterning of Nafion polymer has a range of potential important applications. Applications include Nafion polymer circuits as ionic conductors, protonic transistors,^[45] ionic logic, artificial synapses,^[46] biosymbiotic circuitry, and ion-to-electron transducers in novel integrated circuits and bioelectronics.^[47] Additionally patterning Nafion membranes can increase electrochemical activity and reduce catalyst use in polymer electrolyte membrane fuel cells,^[48] as well as act as an adhesion layer for TDD patterning of SWCNT with high resolution.^[4]

3.1 | Effect of inking speed (dwell time per unit length) on deposited layer thickness

The inking speed (blade coating speed) was hypothesized to affect the deposited layer thickness. Increasing the inking speed can decrease the available time that additional evaporation-driven flow can deposit material at a certain location; thus, reducing the total amount of material deposited in the microchannels and reducing the deposited layer thickness. Conversely, dwell time of the inking droplet per length of microchannel, which is the inverse of the inking speed, should increase the deposited layer thickness. Observing a change in deposited layer thickness due to inking speed/dwell time per unit length supports the claim that evaporation-driven flow significantly contributes to the deposition of ink material into long channels during TDD (Figure 1B). If evaporation-driven flow is adding to the total material deposited, then increased dwell time per unit length should increase the layer thickness within a certain range.^[42,49] If evaporation-driven flow is not present, then changing dwell time per unit length would not affect the total material deposited and result in a horizontal line for the function of deposited layer thickness against dwell time per unit length.

We plotted the data using D instead of inking speed to determine how well Equation 16 models the TDD process. Figure 3 is a plot of experimentally-measured $T^{2/3}$ against D , with the inset displaying an example SEM image of the deposited layers in the microchannels. A quadratic equation of best fit is presented over the data, with the regression analysis displayed in Table 1. This quadratic equation is the same form to the model for deposited layer thickness proposed in quadratic form (Equation 17). We also display the plot and regression analysis for a linear fit in Supporting Information 3 (Figure S1, Table S1).

Equation 17 as a quadratic equation fits the plots of experimentally-determined $T^{2/3}$ against D (Figure 3,

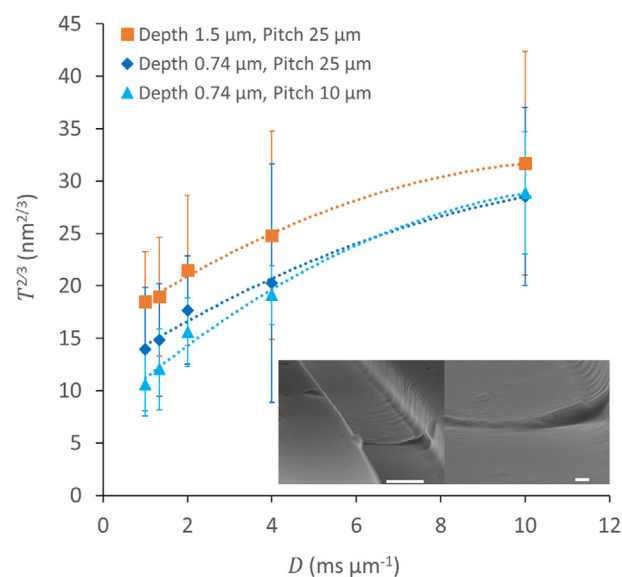


FIGURE 3 Plot of $T^{2/3}$ measured from SEM images against D during TDD deposition of Nafion dispersion in microchannels of $\sim 2.1 \mu\text{m}$ width. Microchannels $\sim 1.5 \mu\text{m}$ depth with $25 \mu\text{m}$ pitch (orange squares), $\sim 0.74 \mu\text{m}$ depth with $25 \mu\text{m}$ pitch (dark blue diamonds) $\sim 0.74 \mu\text{m}$ depth with $10 \mu\text{m}$ pitch (light blue triangles) were used. Curve of the best-fit quadratic relationship is displayed over the data. Error bars are 1 standard deviation. Insets are example SEM images of the deposited layers in the microchannels (Scale bars $1 \mu\text{m}$ left, 100nm right).

Table 1) better than a simple linear relationship (Figure S1, Table S1) with better coefficients of determination ($R^2 > 0.988$). This is not unexpected given the extra fitting parameter, but more importantly, the quadratic equation provides a better fit to the actual physical system and matches the proposed model. The linear fitting suggests that T could increase continuously with D , which clearly cannot be the case given there are limited amounts of material available and the channel has a defined volume that can eventually be filled up. Additionally, the Y-intercepts of the best-fit quadratic relationships derived from the model also support the theoretical understanding. We added an estimate of T_0 /channel depth in Table 1 and Table S1 by dividing Y-int $^{3/2}$ by channel depth (this ignores $\frac{\sqrt{\varphi_0 \langle h \rangle}}{\varphi_{\text{max}} \sqrt{\varphi_g h_0}}$). One of the estimates in Table S1, however, is significantly higher than the theoretical maximum of 5.39%, suggesting the linear relationship model is likely not complete. It can be observed that for the proposed quadratic model, the estimated T_0 /channel depth from the best-fit relationships (Table 1) is at or just below our proposed theoretical maximum of $\sim 5.39\%$ as expected. Experimental conditions of ambient temperature/humidity, initial particle volume fraction in the ink dispersion φ_0 , and initial dispersion viscosity η_0 were kept

TABLE 1 Regression analysis for the best fitting quadratic relationships between $T^{2/3}$ and D during TDD deposition of Nafion dispersion in microchannels of $\sim 2.1 \mu\text{m}$ width

	Depth 1.5 μm , pitch 25 μm	Depth 0.74 μm , pitch 25 μm	Depth 0.74 μm , pitch 10 μm
X ² coefficient ($-\frac{\varphi_0^{1-k} k k_A^2 p_{ev}^2}{A_\eta \eta_0^2 \langle h \rangle \sqrt[3]{\varphi_{max}^2 \varphi_g h_0}}$)	-0.1177	-0.09139	-0.1440
X ² coefficient error	0.03344	0.05809	0.07273
X coefficient ($\frac{\varphi_0^{1-k} k_A p_{ev}}{A_\eta \sqrt[3]{\varphi_{max}^2 \varphi_g h_0}}$)	2.761	2.579	3.545
X coefficient error	0.3823	0.6641	0.8315
Y-intercept (T_0)	15.85	11.84	7.781
Y-intercept error	0.6509	1.131	1.416
Coefficient of determination (R^2)	0.9957	0.9889	0.9888
Baseline thickness (T_0)/channel depth estimate (%)	4.23 ± 0.04	5.53 ± 0.16	2.95 ± 0.23

The estimate for the baseline layer thickness T_0 /channel depth was determined by dividing Y-int^{3/2} by d (ignoring $\frac{\sqrt{\varphi_0 \langle h \rangle}}{\varphi_{max} \sqrt[3]{\varphi_g h_0}}$).

constant for the data in Figure 3, which should keep the X coefficient constant except for the microchannel geometry according to the proposed model (Equation 17). The X² coefficients are all negative, which matches the coefficient for D^2 in the proposed model. This negative coefficient represents the deceleration of the evaporation-driven flow due to the viscosity dampening.

This relation $T \propto (p_{ev} D)^{3/2}$ for the evaporation-driven flow constant we proposed in the model using Equation 17 is different to the relation $T \propto p_{ev} D$ previously modeled and supported by data for thin film blade coating of colloidal dispersions in the evaporative regime.^[40,41,50] This difference in the evaporation-driven flow constant is due to the effect of the internal perpendicular flows C occurring inside the microchannel due to pinning of the droplet at the top edge of the microchannels which does not occur for thin film blade coating. If we isolate C , as shown in Equation 18, the relation $T \propto p_{ev} D$ is observed again, highlighting the fact that C causes a deviation from the relation observed in the system of thin film blade coating of colloidal dispersions in the evaporative regime. Additionally, our data suggests an extra term of viscosity/aggregation dampening that is present for deposition of a material layers within microchannels during TDD and not during thin film blade coating in the evaporative regime, with the additional term having the relation $T \propto (-p_{ev}^2 D^2)^{3/2}$. The appearance of the additional term is due to the additional volume of ink dispersion present over the depositing film due to pinning of the droplet to the top edge of the channel walls. The thin film blade coating has a meniscus contact line at the deposited layer surface which is lower than the contact line pinned at the top edge of the

microchannel. This additional liquid volume allows for a longer evaporation-driven flow to the deposited layer than possible during film blade coating that is eventually slowed by local viscosity dampening.

3.2 | Effect of ink dispersion volume fraction on deposited layer thickness

T was also hypothesized to be dependent on volume fraction of the material in the ink dispersion (φ_0). Simplifying the model in Equation 17 we can obtain

$$T^{2/3} = a \varphi_0 + b \varphi_0^{1-k} \quad (20)$$

where a and b are constant coefficients. The shape of the function, therefore, depends on the value of k . For $k = 1$ and $k = 0$, the function becomes a simple linear relationship where $T^{2/3} \sim \varphi_0$. Theoretically, $k = 0$ should not physically occur though as it implies that viscosity of the ink dispersion does not increase with increasing φ_0 . For $0 < k < 1$ and $k > 1$ within most of the range of positive φ_0 , we also find that $T^{2/3} \sim \varphi_0$. However, at low φ_0 values, the function can deviate from a linear relationship. For $0 < k < 1$ at low φ_0 , the value for $T^{2/3}$ is lower than that expected for a linear relationship, and the y-intercept approaches the origin as $k \rightarrow 0$. Alternatively, for $k > 1$ at low φ_0 , the value for $T^{2/3}$ is higher than that expected for a linear relationship, and $T^{2/3}$ suddenly becomes very large as $\varphi_0 \rightarrow 0$, with an asymptote forming at $\varphi_0 = 0$. Regardless of the value of k , we expect to see a linear relationship ($T^{2/3} \sim \varphi_0$) for most of the positive range of φ_0 .

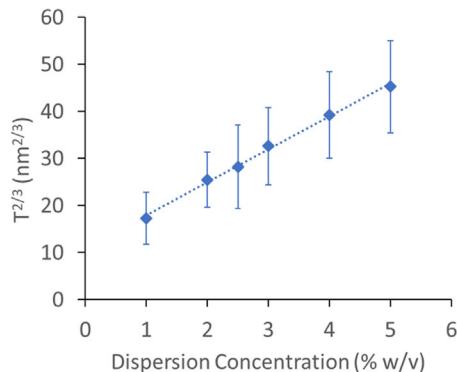


FIGURE 4 Plot of $T^{2/3}$ measured from SEM images against Nafion dispersion concentration during TDD deposition of Nafion dispersion in microchannels of 2.9 μm width, 1.27 μm depth, 30 μm pitch. Linear line of best fit ($R^2 = 0.996$) is displayed over the data. Error bars are 1 standard deviation.

Figure 4 is a plot of the measured $T^{2/3}$ from TDD deposition of Nafion dispersions of varying weight/volume concentrations in 1.27 μm deep, 2.9 μm wide, 30 μm pitch microchannels at 100 $\mu\text{m s}^{-1}$ inking speed. We observed that $T^{2/3}$ for the experimental data was linearly proportional to Nafion concentration as expected with the linear line of best fit having $R^2 = 0.996$. This suggests the model in Equation 17 fits to the data well and accurately predicts the relationship $T^{2/3} \sim \varphi_0$ for the range of φ_0 measured. This relationship may still deviate, however, at very low φ_0 or at much higher k values where $k > 1$.

3.3 | Effect of channel depth and width on deposited layer thickness

The microchannel dimensions (depth d and width w) are expected to affect the deposited layer thickness; however, the relationship is complex. First, d clearly affects the baseline deposited layer thickness T_0 as the average pinned droplet height $\langle h \rangle$ is proportional to d . Second, the channel dimensions will determine the magnitude of the internal flow factor, C . Finally, the microchannel geometry constant k_A depends on d and w .

Figure 5A,B are plots of the measured deposited layer thickness T or $T^{2/3}$, respectively against microchannel depth d from TDD deposition of Nafion dispersion in microchannels with 2.1 μm width, 25 μm pitch at 1000 $\mu\text{m s}^{-1}$ inking speed.

Generally, T increases with d . If we keep $w = 1$ and assume $\langle h \rangle = h_0 = d$ we can simplify k_A as

$$k_A = \frac{d^{5/2}}{16d + 8} \quad (21)$$

and substituting Equation 21 into Equation 16 we get,

$$T = \frac{\varphi_0^{3/2}}{\varphi_{\max} \sqrt{\varphi_g d}} \times \left(d + \frac{d^{5/2} p_{ev} D}{A_\eta (16d + 8) \left(\varphi_0 + \varphi_0 \frac{d^{3/2} p_{ev}}{\eta_0 (16d + 8)} D \right)^k} \right)^{3/2} \quad (22)$$

We can now plot Equation 22 with d as the independent variable with the other variables constant,

$$T = \frac{a}{\sqrt{d}} \left(d + \frac{b d^{5/2}}{(2d + 1) \left(\varphi_0 + \frac{c \varphi_0 d^{3/2}}{(2d + 1)} \right)^k} \right)^{3/2} \quad (23)$$

where $a = \frac{\varphi_0^{3/2}}{\varphi_{\max} \sqrt{\varphi_g}}$, $b = \frac{p_{ev} D}{8 A_\eta}$, and $c = \frac{p_{ev} D}{8 \eta_0}$. We have fit Equation 23 to the experimentally obtained data in Figure 5A (blue curve). We can observe that the model fits the data relatively well. T increasing with d in Figure 5A is reflected in our model with the dependence on d .

If we use Equation 17 instead of Equation 16 to obtain the function of $T^{2/3}$ against d we obtain,

$$T^{2/3} = \frac{\varphi_0}{\sqrt[3]{\varphi_{\max}^2 \varphi_g d}} \times \left(d + \frac{p_{ev}}{A_\eta \varphi_0^k} \frac{d^{5/2}}{16d + 8} D - \frac{k p_{ev}^2}{A_\eta \varphi_0^k \eta_0^2 d} \frac{d^5}{(16d + 8)^2} D^2 \right) \quad (24)$$

$$T^{2/3} = a d^{\frac{2}{3}} + b \left(\frac{d^{\frac{13}{6}}}{2d + 1} \right) - c \left(\frac{d^{\frac{11}{3}}}{(2d + 1)^2} \right) \quad (25)$$

Equation 25 can also fit the experimentally obtained data in Figure 5B (orange curve) well. However, Equation 25 results in decreasing $T^{2/3}$ at increasing d for the higher d region (negative slope tangent), resulting in $T^{2/3} = 0$ at a certain d . This does not match the theoretical description of what is physically occurring. Additionally, Equation 17 is an approximation using Taylor series expansions. Considering these issues, the model in Equation 16 fits the experimental data better and should be used when considering the effects of microchannel depth to the deposited layer thickness.

Figure 6 is a plot of the measured deposited layer thickness T from TDD deposition of Nafion dispersion in

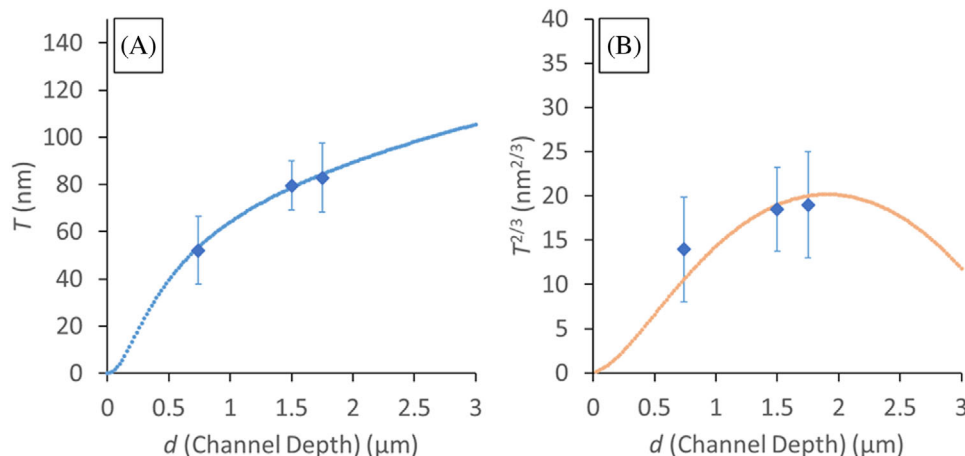


FIGURE 5 Plots of **(A)** T and **(B)** $T^{2/3}$ measured from SEM images against microchannel depth d during TDD deposition of 5% w/v Nafion dispersion in microchannels with constant width (2.1 μm), pitch (30 μm) and inking speed (1000 $\mu\text{m s}^{-1}$). Blue curve in **(A)** is a fitted function from Equation 23, demonstrating the good fit to the model in Equation 16. Orange curve in **(B)** is a fitted function from Equation 25, demonstrating the poor fit to the model in Equation 17. Error bars are 1 standard deviation.

microchannels of varying widths w and constant depth d , pitch/width ratio, and 500 $\mu\text{m s}^{-1}$ (light blue squares) or 50 $\mu\text{m s}^{-1}$ (dark blue diamonds) inking speed.

Generally, T decreases with increasing w . While k_A can be dependent on w , it should be noted that $\langle h \rangle$ and h_0 are also dependent on w . This is due to the fact that contact angle between the pinned droplet contact line at the top edges of the microchannel and the microchannel sidewall is maintained at an equilibrium. As the microchannel gets wider with similar contact angle, the droplet height at the center of the microchannel (h_0) necessarily becomes relatively lower (Figure 6B). If contact angle at the microchannel top edge is held constant, then $h_0 = 0$ at large microchannel widths relative to the depth, resulting in the droplet surface contacting the surface and rupturing the pinned droplet. However, we found experimentally that wider microchannels were still able to maintain pinned droplets without rupture, suggesting that equilibrium contact angle at the top edges of the microchannels is not constant for all microchannel geometries. $\langle h \rangle$ and h_0 are consequently relative to w with the relations,

$$h_0 = d - \frac{w}{2} (\sec \theta - \tan \theta) \quad (26.1)$$

$$\langle h \rangle = d - \frac{w}{4} \left(\left(\frac{\pi}{2} - \theta \right) \sec^2 \theta - \tan \theta \right) \quad (26.2)$$

where θ is the contact angle of the pinned droplet relative to the microchannel sidewall. This is derived from assuming the profile of the pinned droplet surface matches an arc of a circle. See *Supporting Information 4* for full derivation. θ can be calculated in radians as

$$\theta = \frac{\pi}{2} - \theta_r A_\theta w/d \quad (26.3)$$

where θ_r is the baseline contact angle reduction under a flat 90° contact angle and A_θ is the contact angle change coefficient with a power factor of the microchannel aspect ratio w/d .

Substituting k_A from Equation 4 into the model in Equation 16 we can obtain

$$T = \frac{a}{\sqrt{h_0}} \left(\langle h \rangle + \frac{b \langle h \rangle w^{5/2}}{(2d+w) \left(\varphi_0 + \varphi_0 c \frac{\langle h \rangle^{3/2} w^{5/2}}{(2d+w)} \right)^k} \right)^{3/2} \quad (27)$$

where $a = \frac{\varphi_0^{3/2}}{\varphi_{\max} \sqrt{\varphi_g}}$, $b = \frac{p_{ev} D}{8 A_\eta}$, and $c = \frac{p_{ev} D}{8 \eta_0}$. We can plot Equation 27 using Equations 26.1-26.3 with w as the independent variable and other variables constant to determine the effect of w on the model in Equation 16. Curves of best fit using Equation 27 have been plotted in Figure 6A to compare with the experimental data. We used known values of $d = 1150$ nm, $\varphi_0 = 0.0539$, and $a \approx 0.022$ ($\varphi_g \approx 0.3$ and $\varphi_{\max} \approx 1$),^[38] and we used common values $\theta_r = \frac{\pi}{4}$ and $A_\theta = 0.9$. Fitting the model to the data, we found that b and c were ~ 10 times larger when fitting the model to the data for inking speed 50 $\mu\text{m s}^{-1}$ compared to fitting the model to the data for inking speed 500 $\mu\text{m s}^{-1}$. This is consistent with the model as $b \propto D$ and $c \propto D$, and D is 10 times larger for inking speed 50 $\mu\text{m s}^{-1}$ compared to 500 $\mu\text{m s}^{-1}$. The only main difference is that $k = 1.25$ when fitting the model to the data for inking speed 50 $\mu\text{m s}^{-1}$ compared to $k = 1.31$ when fitting to inking speed 500 $\mu\text{m s}^{-1}$. This difference may just be within experimental error. Regardless, both values for k are similar to that recently reported by Gupit et al. for Nafion dispersions in water/alcohol

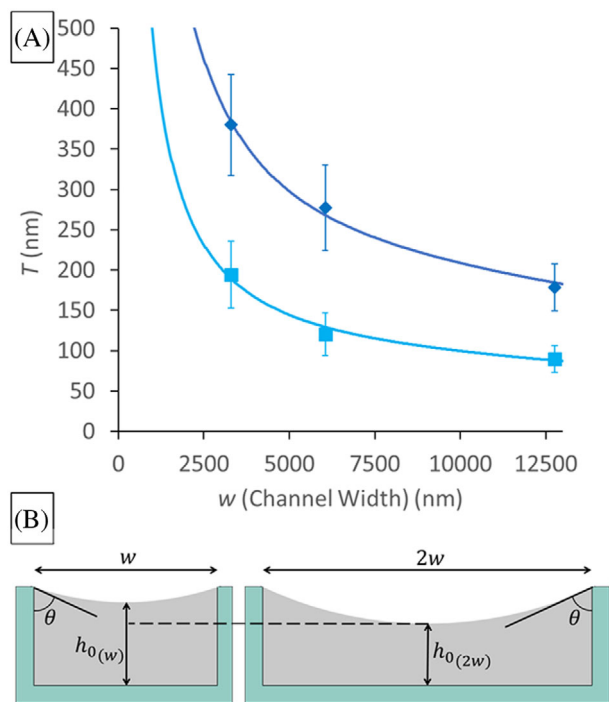


FIGURE 6 **(A)**, Plot of T measured from SEM images against w during TDD deposition of 5% w/v Nafion dispersion in microchannels with constant depth (1.15 μm), pitch/width ratio (10) and inking speed (light blue squares 500 $\mu\text{m s}^{-1}$, dark blue diamonds 50 $\mu\text{m s}^{-1}$). Error bars are 1 standard deviation. Curves are a fitted function from Equation 27, demonstrating the fit to the model in Equation 16. Common values of constants used were $d = 1150$, $a = 0.022$, $\varphi_0 = 0.0539$, $\theta_r = \frac{\pi}{4}$, $A_\theta = 0.9$. The curve fitted to the data for inking speed 50 $\mu\text{m s}^{-1}$ had constants $b = 10052$, $c = 4.539$, $k = 1.25$ with root mean square 6.74. The curve fitted to the data for inking speed 500 $\mu\text{m s}^{-1}$ had constants $b = 1005.2$, $c = 0.4539$, $k = 1.31$ with root mean square 6.03. **(B)**, Diagram demonstrating that as w increases with similar contact angle of the pinned droplet at the top edge of microchannel, h_0 will decrease and consequently T will decrease

solvents within the relevant particle volume fraction ranges ($k = 1.25$).^[38]

While the microchannel geometry does affect T through k_A , the measured data also shows that the microchannel geometry has a significant effect on the internal flows, C , like Marangoni flows or capillary flows, and consequently a significant effect on the deposited layer morphology and T . This is understandable considering the droplet is pinned to the top of the microchannel sidewalls for a long period during evaporation. The droplet contact line will stay pinned to the channel top edge during evaporation of the ink solvent, until the contact angle with respect to the channel wall is equal or lower than the RCA of the droplet on the channel wall surface. Then the contact line begins to slip down the sidewall, or the sagging middle of the pinned droplet connects with the microchannel floor. During this

time, internal capillary flows will continually deposit more materials to the sidewalls, away from the center of the microchannel. When we tried to fit the data to the model while ignoring the effect of C (using Equation 11 without C), we found that T will always be increasing with w . This does not match the experimental data in Figure 6A which shows T decreasing with w . This demonstrates that incorporating C is critical to effectively model the system experimentally measured in this work and many other functional material ink dispersion systems.

3.4 | Effect of channel pitch on deposited layer thickness

While doing the previous experiments we found that the pitch between the microchannels also appears to have an effect on the deposited layer thickness T with decreased pitch resulting in decreased T . This may be caused by the interacting flow around the microchannels in the main dragged droplet near the droplet contact line (Figure 7). Reduced pitch means the flow into neighboring microchannels will interact more and potentially interfere with each other, limiting the flow of material into the microchannels and limiting the total material deposited into microchannels with reduced pitch (Figure 7B). Each microchannel will reduce pressure within the main droplet near the pinned droplet/main droplet interface, due to the increase in local fluid velocity as liquid dispersion is driven into the microchannels (Bernoulli principle). If the microchannels are close to each other, they will lower the liquid pressure near each other's pinned droplet/main droplet interface; thus, reducing the evaporation-driven pressure gradient p_{ev} , hence reducing the evaporation-driven flow into the microchannels. This effect tapers off as the distance increases between each microchannel (pitch increases).

We explored the effect on T by varying the microchannel pitch. Figure 8A is a plot of the measured deposited layer thickness T from TDD deposition of Nafion dispersions in microchannels of varying pitch/width ratio (λ) and constant depth (d), width (w), and 1000 $\mu\text{m s}^{-1}$ (orange squares) or 100 $\mu\text{m s}^{-1}$ (dark blue diamonds) inking speed. T increases with λ , and tapers off to approach a certain T at higher λ . This is expected from the theoretical perspective as the effect of lowering pressure becomes negligible at high λ . Additionally, at higher inking speeds, thickness approaches T_0 as the evaporation-driven flow has less of an effect. Consequently, this should result in pitch having less of an effect on thickness and the plot of thickness against pitch approaching a horizontal line (flattening). This can be observed in Figure 8A as the data for higher inking speed (1000 $\mu\text{m s}^{-1}$)

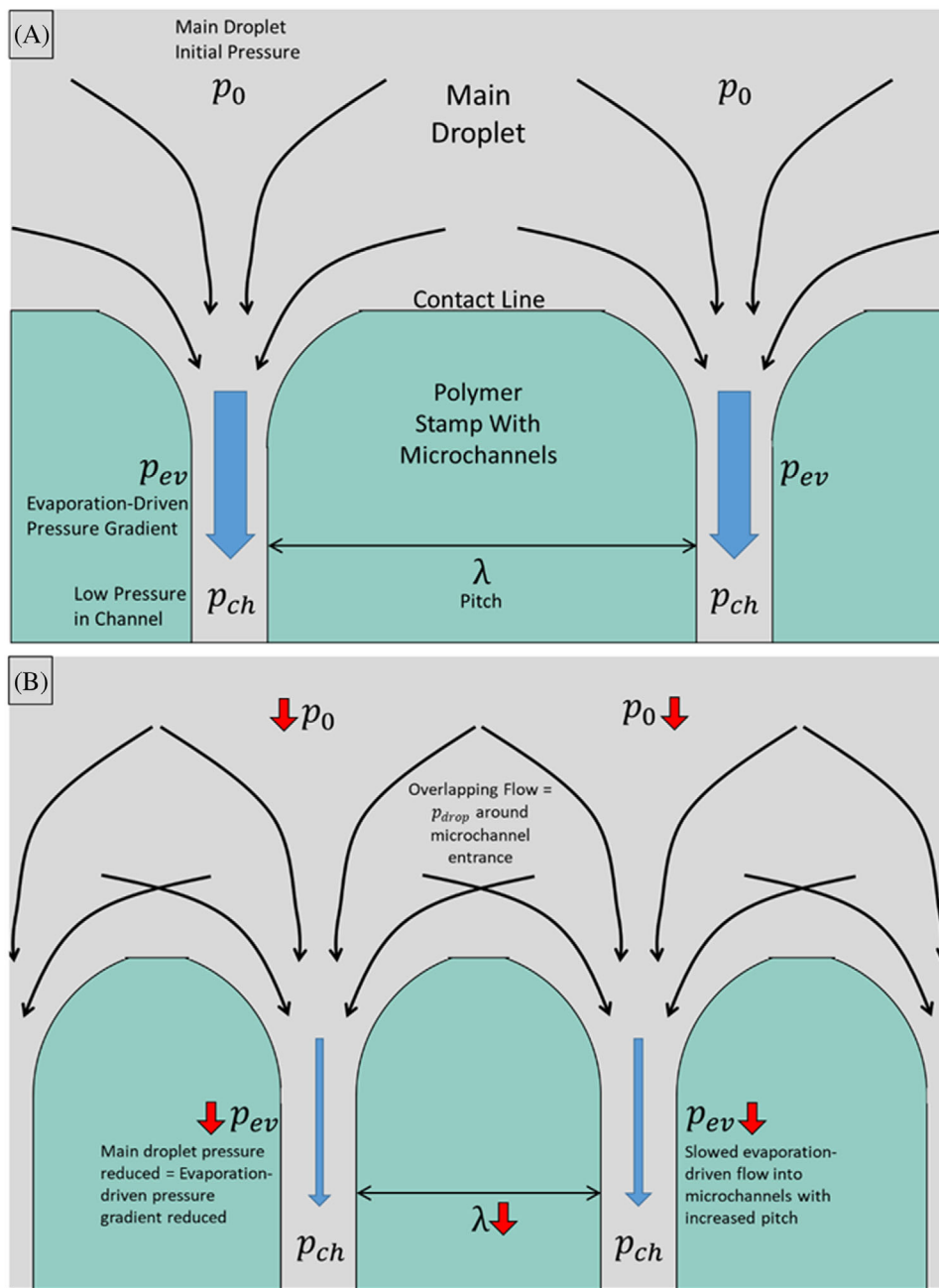


FIGURE 7 Diagram of physical process near the main dragged droplet contact line during TDD deposition of dispersions into microchannels. Top down view over contact line. **(A)** Process with large pitch that has high evaporation-driven pressure gradient and **(B)** process with reduced pitch which results in reduced pressure near the pinned droplet/main droplet interface of adjacent microchannels and consequently reduced pressure gradient in the microchannels.

has a flatter curve approaching a horizontal line. Fitting a quadratic curve of best fit shows a good fit with $R^2 = 0.99$ and $R^2 = 0.97$ for the $1000 \mu\text{m s}^{-1}$ (orange squares) and $100 \mu\text{m s}^{-1}$ (dark blue diamonds) inking speed, respectively, implying a $T \propto \lambda - \lambda^2$ relationship. However, as $\lambda \rightarrow \infty$, T should approach a certain value as there is no adjacent microchannel to interfere with the evaporation-driven flow. This means that the quadratic relationship fails after a certain range. We propose another relationship

between T and λ . First, we can define p_{ev} now as,

$$p_{ev} = p_0 - \frac{p_{drop}}{\sqrt[3]{\lambda}} \quad (28)$$

where p_0 is the evaporation-driven pressure gradient for a single isolated microchannel, p_{drop} is the pressure drop due to adjacent microchannel outlets. When $\lambda \rightarrow \infty$ as for a single isolated microchannel, then $p_{ev} = p_0$, ie: no

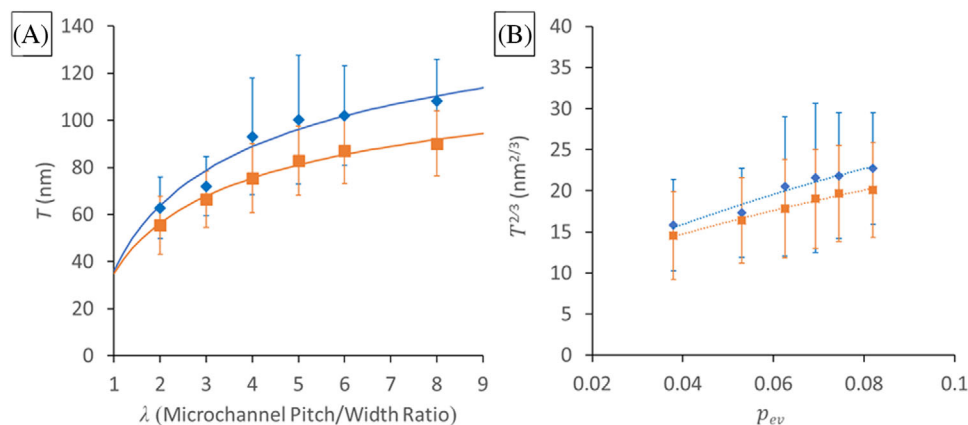


FIGURE 8 **(A)** Plot of T measured from SEM images against microchannel pitch/width ratio λ during TDD deposition of 5% w/v Nafion dispersion in microchannels with constant depth ($1.75 \mu\text{m}$), width ($4.67 \mu\text{m}$) and inking speed (orange squares $1000 \mu\text{m s}^{-1}$, blue diamonds $100 \mu\text{m s}^{-1}$). Error bars are 1 standard deviation. Curves are a fitted function from Equation 29, demonstrating the fit to the model in Equation 16. Common values of constants used was $d = 1750$, $w = 4670$, $a = 0.022$, $\varphi_0 = 0.0539$, $\theta_r = \frac{\pi}{4}$, $A_\theta = 0.9$, $p_0 \approx 0.157$, $p_{drop} = 0.15$. The curve fitted to the data for inking speed $100 \mu\text{m s}^{-1}$ had constants $b = 546.3$, $c = 170$, $k = 1.25$ with root mean square 3.82. The curve fitted to the data for inking speed $1000 \mu\text{m s}^{-1}$ had constants $b = 54.63$, $c = 17.0$, $k = 1.96$ with root mean square 1.96. **(B)** Plot of $T^{2/3}$ against $p_{ev} = p_0 - \frac{p_{drop}}{\sqrt[3]{\lambda}}$ with the same data as in **(A)**. Curves of the best-fit quadratic relationship are displayed over the data as a fit of the model in Equation 17. Error bars are 1 standard deviation.

pressure drop. When $\lambda \rightarrow 1$, then $p_{ev} = p_0 - p_{drop}$. Then $\lambda = 1$ is equated to microchannels covering the whole substrate area, which can be compared to thin film blade coating in the evaporative regime. Substituting Equation 28 into the model in Equation 16 we can obtain

$$T = \frac{a}{\sqrt{h_0}} \left(\langle h \rangle + \frac{b \left(p_0 - \frac{p_{drop}}{\sqrt[3]{\lambda}} \right)}{\left(\varphi_0 + \frac{c \varphi_0}{\langle h \rangle} \left(p_0 - \frac{p_{drop}}{\sqrt[3]{\lambda}} \right) \right)^k} \right)^{3/2} \quad (29)$$

where $a = \frac{\varphi_0^{3/2}}{\varphi_{max} \sqrt{\varphi_g}}$, $b = \frac{k_A D}{A_\eta}$, and $c = \frac{k_A D}{\eta_0}$. We can plot Equation 29 using Equations 26.1-26.3 and Equation 28 with λ as the independent variable and other variables constant to determine the effect of λ on the model in Equation 16. Curves of best fit using Equation 29 have been plotted in Figure 8A to compare with the experimental data. We used known values of $d = 1750 \text{ nm}$, $w = 4670 \text{ nm}$, $\varphi_0 = 0.0539$, and $a \approx 0.022$ ($\varphi_g \approx 0.3$ and $\varphi_{max} \approx 1$),^[38] and we used common values $\theta_r = \frac{\pi}{4}$ and $A_\theta = 0.9$. The fitted curves show a good fit to the data. We found that the model fits both data sets even with the same value of $p_0 \approx 0.157$, consistent with the theory of the model. We found again that b and c were ~ 10 times larger when fitting the model to the data for inking speed $100 \mu\text{m s}^{-1}$ compared to $1000 \mu\text{m s}^{-1}$. This is consistent with the model and what we found when fitting the model to the data for varying microchannel widths (Figure 6A). Again we found that the only

changing variable is k with $k \approx 1.25$ when fitting the model to the data for inking speed $100 \mu\text{m s}^{-1}$ compared to $k \approx 1.96$ when fitting to inking speed $1000 \mu\text{m s}^{-1}$. k is consistently higher for higher inking speeds (lower D) and lower inking speeds approach the expected value of $k = 1.25$ from recent literature.^[38] This suggests that k can be dependent on D and can deviate from expected values for higher inking speeds. This difference may be due to the higher inking speeds causing the dispersed particles to experience a higher “virtual” viscosity. The necessarily increased flow rate of the ink dispersion at higher inking speed results in less than φ_0 volume of particles carried with the solvent from the main droplet into the microchannels, as the smaller solvent molecules replace a higher proportion of the volume lost to evaporation in the microchannel. The dispersed particles travel more slowly into the microchannels than expected for a homogenous liquid/solution with the same viscosity/concentration profile, and thus just the dispersed particles (not the solvent) experience a higher “virtual” viscosity, and an increased k value.

Figure 8B is a plot of the same experimental data as in Figure 8A except with $T^{2/3}$ against $p_{ev} = p_0 - \frac{p_{drop}}{\sqrt[3]{\lambda}}$ as the independent variable and a quadratic function fitted to the data instead to compare with the model in Equation 17. A quadratic relationship fits the data well with $R^2 = 0.95$ and $R^2 = 0.99$ for the $100 \mu\text{m s}^{-1}$ (dark blue diamonds) and $1000 \mu\text{m s}^{-1}$ (orange squares) inking speed, respectively. The same R^2 is achieved regardless of the value of p_{drop} . The good fit of the models in Equations 16 and 17 with the measured data when using Equation 28 suggests that

theoretically-derived Equation 28 reflects the relationship between p_{ev} and λ .

The proposed model supported by the data is important to obtain good control of the thickness and morphology of the deposited layers patterned using the novel TDD patterning technique.^[1,2,4,6] Control of all the dimensions during patterning of materials is critical for manufacturing to improve the quality and reliability of the technique and devices manufactured from it. Previous studies have only briefly outlined the colloidal ink printing mechanism^[1,7] or the conditions to ensure accurate filling of the microchannels.^[6] The findings of this work are, therefore, critical to better understand the technique so it can mature into a commercially-viable advanced nanoscale printing technology. The discovered viscosity dampening effect is unique to TDD of microchannels, which has not previously been observed in thin film blade coating of colloidal dispersions in the evaporative regime^[40,41,50] or surface chemistry-based discontinuous dewetting patterning.^[15–17] Additionally, the effect of pitch is also unique to this technique and is critical to understand for applications. These phenomena will be important to consider when using this patterning technique for advanced manufacturing of devices, as well as guide other techniques that may rely on the flow of colloids through micro/nanoscale channels. Future work will focus on more specifically determining the relationship between the microchannel dimensions and the internal flows (capillary flow and Marangoni flow), and the pinned droplet surface curvature on the resulting deposited layer morphology/thickness.

4 | CONCLUSIONS

This work reports an accurate model for determination of the thickness, T , of the layer deposited in microchannels during TDD of colloidal ink dispersions. The model is supported by the experimentally-measured data and conforms to the theoretical understanding of the system including the theoretical contributions from the baseline layer thickness, evaporation-driven flow, and internal flows (“coffee-ring” effect capillary and Marangoni). We found that the contribution of evaporation-driven flow and internal flows to the deposited layer thickness was significant, with a relation of $T \propto (p_{ev} D)^{3/2}$ for the evaporation-driven flow constant that is different to that previously determined for thin film blade coating of colloidal dispersions in the evaporative regime. Additionally, a unique viscosity/aggregation dampening effect for the system was predicted in the model and observed in the data that is not present in thin film blade coating models. Viscosity dampening slows the evaporation-driven flow over time due to

local increase in viscosity in the microchannels. Ink particle volume fraction/dispersion concentration was linearly proportional to the deposited layer thickness as hypothesized. Increasing microchannels width and depth resulting in a decreased or increased deposited layer thickness, respectively. This is due to the change in flow profile and the change in the effect of internal flows like Marangoni and capillary flows due to microchannel geometry. Interestingly, we found increasing microchannel pitch was found to decrease thickness due to cumulative lowering pressure within the dragged dispersion droplet near adjacent microchannels, and consequently a decreased evaporation-driven pressure gradient. This new understanding of the effect of processing parameters on the resulting thickness and morphology of the deposited layers of functional materials will be critical to enable the fabrication of consistent and high-quality advanced devices from functional materials using the TDD patterning technique.

5 | EXPERIMENTAL SECTION

5.1 | Preparation of Nafion ink dispersions

5% w/v (~5.39% v/v) Nafion 117 dispersions (45% water, 50% lower aliphatic alcohols, Sigma-Aldrich) was used as purchased for depositing Nafion layer in microchannels as a Nafion ink dispersion. 1%-5% w/v diluted Nafion dispersions were prepared by diluting 5% w/v Nafion dispersions with 47:53 water:ethanol mixture and sonicated for 5 minutes to equilibrate. The water:ethanol mixture was used for dilution in order to maintain same proportion of alcohol to water as the commercial dispersion so that evaporation rate remains consistent. All Nafion dispersions were stored in a 4°C fridge and used within 30 minutes of removal from the fridge.

5.2 | Preparation of polydimethylsiloxane (PDMS) microchannel substrates

Si/SiO_x wafer substrates were patterned with a Cr mask using standard photolithography procedures. The non-protected areas on the wafer were etched using reactive ion etching and the Cr mask was then chrome etched. This left a pure silicon wafer with raised line pattern features on an etched background to be used as a mold for casting PDMS. The wafer was coated with a monolayer by placing the wafer under vacuum with a few drops of tridecafluoro-1,1,2,2-tetrahydrooctyl-1-trichlorosilane (TFOCS). The monolayer ensures the cast PDMS does not stick to the silicon wafer to ensure feature fidelity and reuse of the silicon mold.

PDMS microchannel substrates were fabricated by casting PDMS onto the silicon wafer mold. 10:1 Sylgard-184 prepolymer:curing agent was mixed for 3 minutes and poured onto the silicon wafer mold. PDMS was placed under vacuum for 20 minutes to degas and then cured at 80°C for 3 hours. The PDMS was removed from wafer carefully, revealing a cured PDMS stamp with microchannels molded on the top surface from the raised features on the wafer mold. The PDMS microchannel substrates were used as is. Channel dimensions tested were 2.1-12.76 μm width, 0.74-1.75 μm depth, and 10-120 μm pitch.

5.3 | Topographical discontinuous dewetting (TDD) deposition of Nafion layer in PDMS microchannels

A layer of Nafion was deposited from a Nafion ink dispersion into the microchannels on the PDMS substrates by TDD. The PDMS microchannel substrate was moved at a constant speed by a computer-controlled motorized stage while a glass slide inking blade was held ~ 1 mm above the moving microchannels. A droplet of Nafion dispersion was placed between and in contact with the inking blade and the PDMS microchannels substrate, forming a bridge between them. The droplet with polar solvents wets the glass inking blade better than the PDMS substrate, allowing the droplet to stay wetted to the glass inking blade edge and slide over the PDMS if they are moving relative to each other. The droplet was subsequently dragged parallel to the channel direction over the PDMS substrate surface, and the PDMS microchannels were selectively filled with the Nafion dispersion through the TDD process without leaving any Nafion deposited on the non-channel parts of the surface. The inking blade does not touch the stamp; it simply pulls the droplet through surface tension. The inking was done at ambient conditions and the PDMS substrates were dried in ambient air overnight to ensure evaporation of the solvent from the deposited Nafion layers in the microchannels. Inking speeds of 50-1000 $\mu\text{m s}^{-1}$ (3-60 mm min^{-1}) or dwell times per unit length of 0.5-10 $\text{ms } \mu\text{m}^{-1}$ were tested to deposit Nafion layers in microchannels with a variety of dimensions using Nafion dispersions with a range of concentrations (1-5% w/v).

5.4 | Scanning electron microscopy (SEM) characterization of deposited Nafion layers

The PDMS microchannels with deposited Nafion layers were cut by a razor blade at a similar position in each sample to expose the substrate cross section. The sam-

ple cross sections were mounted and dried overnight at 70°C to degas. A carbon coating of ~ 5 nm and platinum coating of ~ 5 nm was deposited on sample cross sections to provide conduction. Secondary electron SEM images were obtained of the cross sections (examples in Supporting Information 5). More than three images of different microchannels were taken of each sample to characterize the cross sections of deposited Nafion layers. Thicknesses of the deposited Nafion layers were determined by measuring the distance from the top of the deposited layer to the microchannel bottom surface at three to four different points at the center of the microchannel. Thicknesses were measured on six to ten different images/microchannels to obtain an average thickness and standard deviation from 18-40 individual measurements per sample. Error bars on all plots represent 1 standard deviation. The measurements on the images were taken using ImageJ image analysis computer program.

5.5 | Rheological characterization of Nafion dispersions

A concentrated Nafion dispersion ($\sim 16.4\%$ w/v) was prepared by evaporating the 5% w/v Nafion 117 dispersion (Sigma-Aldrich) for ~ 4 hours until 1/5 the initial volume remained. Rheological characterization of the concentrated ($\sim 16.4\%$ w/v) and standard ($\sim 5.14\%$ w/v) Nafion dispersions as well as a binary solvent control was performed using a TA Instruments AR-G2 rheometer. Shear rate sweep was performed over range 0.1-1000 s^{-1} with 30 seconds stabilization and 30 seconds measurement each point. Constant 25°C temperature for all measurements.

ACKNOWLEDGMENTS

A. Corletto would like to thank the Australian Government for support through the Research Training Program (RTP) and the support of the Australian Research Council Discovery Program (DP 200101217) is gratefully acknowledged. The authors acknowledge the use of the Queensland node of the Australian National Fabrication Facility (ANFF-Q) at The University of Queensland and the scientific and technical assistance, of the Microscopy Australia Facility at the Center for Microscopy and Microanalysis, The University of Queensland.

CONFLICT OF INTEREST

The authors declare no conflict of interest.

FUNDING SOURCES

This research was sponsored by Australian Research Council (ARC) through Discovery project DP 200101217.

This research is supported by an Australian Government Research Training Program (RTP) Scholarship.


AUTHOR CONTRIBUTIONS


A. Corletto conducted all experiments. A. Corletto wrote manuscript with contributions from J. Shapter. All authors have given approval to the final version of the manuscript.

DATA AVAILABILITY STATEMENT

The data that support the findings of this study are available from the corresponding author upon reasonable request.

ORCID

Alexander Corletto  <https://orcid.org/0000-0001-6021-923X>

Joseph G. Shapter  <https://orcid.org/0000-0002-4000-2751>

REFERENCES

- J. K. Hwang, S. Cho, J. M. Dang, E. B. Kwak, K. Song, J. Moon, M. M. Sung, *Nat. Nanotechnol.* **2010**, *5*(10), 742.
- D. Song, A. Mahajan, E. B. Secor, M. C. Hersam, L. F. Francis, C. D. Frisbie, *ACS Nano* **2017**, *11*(7), 7431.
- A. R. Naik, J. J. Kim, Ö. Usluer, D. L. Gonzalez Arellano, E. B. Secor, A. Facchetti, M. C. Hersam, A. L. Briseno, J. J. Watkins, *ACS Appl. Mater. Interfaces* **2018**, *10*(18), 15988.
- A. Corletto, J. G. Shapter, *ACS Appl. Nano Mater.* **2020**, *3*(8), 8148.
- J. H. Lee, C. H. Kim, K. M. Ho, K. Constant, *Adv. Mater.* **2005**, *17*(20), 2481.
- M. E. Deagen, L. S. Schadler, C. K. Ullal, *ACS Appl. Mater. Interfaces* **2017**, *9*(41), 36385.
- R. J. Jackman, D. C. Duffy, E. Ostuni, N. D. Willmore, G. M. Whitesides, *Anal. Chem.* **1998**, *70*(11), 2280.
- K. S. Park, B. Cho, J. Baek, J. K. Hwang, H. Lee, M. M. Sung, *Adv. Funct. Mater.* **2013**, *23*(38), 4776.
- K. S. Park, S. M. Salunkhe, I. Lim, C. G. Cho, S. H. Han, M. M. Sung, *Adv. Mater.* **2013**, *25*(24), 3351.
- B. Cho, K. S. Park, J. Baek, H. S. Oh, Y. E. Koo Lee, M. M. Sung, *Nano Lett.* **2014**, *14*(6), 3321.
- K. S. Park, K. S. Lee, C. m. Kang, J. Baek, K. S. Han, C. Lee; Y. E. Koo Lee, Y. Kang, M. M. Sung, *Nano Lett.* **2015**, *15*(1), 289.
- K. S. Park, K. S. Lee, J. Baek, L. Lee, B. H. Son, Y. E. Koo Lee, Y. H. Ahn, W. I. Park, Y. Kang, M. M. Sung, *Angew. Chem. Int. Ed. Engl.* **2016**, *55*(35), 10273.
- Y. Park, J. W. Jung, H. Kang, J. Seth, Y. Kang, M. M. Sung, *Nano Lett.* **2019**, *19*(2), 1028.
- S. Pan, H. Zou, A. C. Wang, Z. Wang, J. Yu, C. Lan, Q. Liu, Z. L. Wang, T. Lian, J. Peng, Z. Lin, *Angew. Chem. Int. Ed.* **2020**, *59*(35), 14942.
- D. Tian, Y. Song, L. Jiang, *Chem. Soc. Rev.* **2013**, *42*(12), 5184.
- X. Zhang, J. Jie, W. Deng, Q. Shang, J. Wang, H. Wang, X. Chen, X. Zhang, *Adv. Mater.* **2016**, *28*(13), 2475.
- Y. Lin, Z. Wu; M. Zhang, J. Wu, W. Wen, *Adv. Mater. Interfaces* **2018**, *5*(19), 1800729.
- A. Corletto, J. G. Shapter, *Adv. Sci.* **2020**, *n/a*(n/a), 2001778.
- G. Grau, J. Cen, H. Kang, R. Kitsomboonloha, W. J. Scheideler, V. Subramanian, *Flex. Print. Electron.* **2016**, *1*(2), 023002.
- G. Grau, V. Subramanian, *Flex. Print. Electron.* **2020**, *5*(1), 014013.
- K. K. Price, A. V. McCormick, L. F. Francis, *Langmuir* **2012**, *28*(28), 10329.
- Q. Cao, S. j. Han, G. S. Tulevski, Y. Zhu, D. D. Lu, W. Haensch, *Nat. Nanotechnol.* **2013**, *8*, 180.
- D. K. Paul, K. Karan, A. Docoslis, J. B. Giorgi, J. Pearce, *Macromolecules* **2013**, *46*(9), 3461.
- S. Lone, J. M. Zhang, I. U. Vakarelski, E. Q. Li, S. T. Thoroddsen, *Langmuir* **2017**, *33*(11), 2861.
- T. Kraus, L. Malaquin, H. Schmid, W. Riess, N. D. Spencer, H. Wolf, *Nat. Nanotechnol.* **2007**, *2*(9), 570.
- S. Ni, J. Leemann, H. Wolf, L. Isa, *Faraday Discuss.* **2015**, *181*(0), 225.
- J. Kang, C. G. Park, S. H. Lee, C. Cho, D. G. Choi, J. Y. Lee, *Nanoscale* **2016**, *8*(21), 11217.
- V. Flauraud, M. Mastrangeli, G. D. Bernasconi, J. Butet, D.T.L. Alexander, E. Shahrabi, O.J.F. Martin, J. Brugger, *Nat. Nanotechnol.* **2017**, *12*(1), 73.
- R.D. Deegan, O. Bakajin, T. F. Dupont, G. Huber, S. R. Nagel, T. A. Witten, *Nature* **1997**, *389*, 827.
- P. Kolliopoulos, K. S. Jochem, R. K. Lade, L. F. Francis, S. Kumar, *Langmuir* **2019**, *35*(24), 8131.
- D. Mampallil, H. B. Eral, *Adv. Colloid Interface Sci.* **2018**, *252*, 38.
- R. K. Lade, K. S. Jochem, C. W. Macosko, L. F. Francis, *Langmuir* **2018**, *34*(26), 7624.
- H. Hu, R. G. Larson, *J. Phys. Chem. B* **2006**, *110*(14), 7090.
- R. G. Larson, *AIChE J.* **2014**, *60*(5), 1538.
- M. Bahrami, M. M. Yovanovich, J. R. Culham, *J. Fluids Eng.* **2006**, *128*(5), 1036.
- M. Akbari, D. Sinton, M. Bahrami, *J. Fluids Eng.* **2009**, *131*(4).
- A. Tamayol, M. Bahrami, *J. Fluids Eng.* **2010**, *132*(11).
- C. I. Gupit, X. Li, R. Maekawa, N. Hasegawa, H. Iwase, S. Takata, M. Shibayama, *Macromolecules* **2020**, *53*(4), 1464.
- T. Okuzono, M. Kobayashi, M. Doi, *Physical Review E* **2009**, *80*(2), 021603.
- F. Doumenc, B. Guerrier, *Langmuir* **2010**, *26*(17), 13959.
- F. Doumenc, J. B. Salmon, B. Guerrier, *Langmuir* **2016**, *32*(51), 13657.
- X. Gu, L. Shaw, K. Gu, M. F. Toney, Z. Bao, *Nat. Commun.* **2018**, *9*(1), 534.
- S. P. Meeker, W.C.K. Poon, P. N. Pusey, *Phys. Rev. E* **1997**, *55*(5), 5718.
- P. J. Yunker, T. Still, M. A. Lohr, A. G. Yodh, *Nature* **2011**, *476*(7360), 308.
- A. M. Deml, A. L. Bunge, M. A. Reznikov, A. Kolessov, R. P. O'Hayre, *J. Appl. Phys.* **2012**, *111*(7), 074511.
- Y. van de Burgt, E. Lubberman, E. J. Fuller, S. T. Keene, G. C. Faria, S. Agarwal, M. J. Marinella, A. Alec Talin, A. Salleo, *Nat. Mater.* **2017**, *16*(4), 414.
- J. G. Gluschke, J. Seidl, R. W. Lyttleton, K. Nguyen, M. Lagier, F. Meyer, P. Krogstrup, J. Nygård, S. Lehmann, A. B. Mostert, P. Meredith, A. P. Micolich, *Mater. Horiz.* **2020**.
- Y. Jeon, D. J. Kim, J. K. Koh, Y. Ji, J. H. Kim, Y. G. Shul, *Sci. Rep.* **2015**, *5*(1), 16394.
- L. Landau, B. Levich, Dragging of a liquid by a moving plate. In *Dynamics of Curved Fronts*, P. Pelcé, Ed. San Diego: Academic Press, **1988**; pp 141.

50. G. Jing, H. Bodiguel, F. Doumenc, E. Sultan, B. Guerrier, *Langmuir* **2010**, *26*(4), 2288.

SUPPORTING INFORMATION

Additional supporting information may be found online in the Supporting Information section at the end of the article.

How to cite this article: Corletto A, Shapter JG. Thickness/morphology of functional material patterned by topographical discontinuous dewetting. *Nano Select.* **2021**;2:1723–1740. <https://doi.org/10.1002/nano.202000301>